ACS APPLIED ELECTRONIC MATERIALS

pubs.acs.org/acsaelm

Forum Article

Engineering of Thermoelectric Composites Based on Silver Selenide in Aqueous Solution and Ambient Temperature

Bingfei Nan, Mengyao Li, Yu Zhang,* Ke Xiao, Khak Ho Lim, Cheng Chang, Xu Han, Yong Zuo, Junshan Li, Jordi Arbiol, Jordi Llorca, Maria Ibáñez, and Andreu Cabot*

Cite This: https://doi.org/10.1021/acsaelm.3c00055

Read Online

ACCESS | Metrics & More | Article Recommendations | Supporting Information

ABSTRACT: The direct, solid state, and reversible conversion between heat and electricity using thermoelectric devices finds numerous potential uses, especially around room temperature. However, the relatively high material processing cost limits their real applications. Silver selenide (Ag_2Se) is one of the very few n-type thermoelectric (TE) materials for room-temperature applications. Herein, we report a room temperature, fast, and aqueous-phase synthesis approach to produce Ag_2Se, which can be extended to other metal chalcogenides. These materials reach TE figures of merit (zT) of up to 0.76 at 380 K. To improve these values, bismuth sulfide (Bi_2S_3) particles also prepared in an aqueous solution are incorporated into the Ag_2Se matrix. In this way, a series of Ag_2Se/Bi_2S_3 composites with Bi_2S_3 wt % of 0.5, 1.0, and 1.5 are prepared by solution blending and hot-press sintering. The presence of Bi_2S_3 significantly improves the Seebeck coefficient and power factor while at the same time decreasing the thermal conductivity with no apparent drop in electrical conductivity. Thus, a maximum zT value of 0.96 is achieved in the composites with 1.0 wt % Bi_2S_3 at 370 K. Furthermore, a high average zT value (zT_{ave}) of 0.93 in the 300−390 K range is demonstrated.

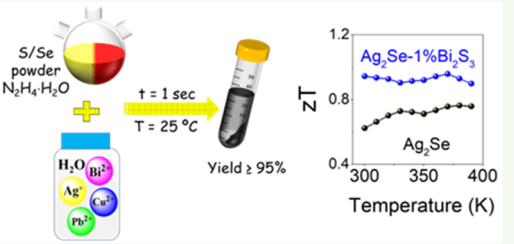

KEYWORDS: *thermoelectricity, silver selenide, aqueous synthesis, bismuth sulfide, composite*

INTRODUCTION

Thermoelectric (TE) devices allow for direct, solid state, and reversible conversion between heat and electricity.[1−4] TE devices can harvest heat from the ambient environment, potentially increasing the efficiency of a plethora of processes. They also allow precise control of the temperature and effective cooling of hot spots. However, their real-world applications are limited to several niche markets due to their relatively low cost-effectiveness. The high cost of TE devices is related to the use of scarce elements such as Te, the need for high-temperature or vacuum-based processes for the synthesis of TE materials, and the quasimanual manufacturing of TE modules. Alternative printing technologies are being developed worldwide, but the use of organic solvents for the synthesis of the materials and/or the ink formulation is still a major drawback to the environmentally friendly and low-cost processing of TE devices. On top of the high cost, the energy conversion efficiency of TE devices is relatively low. The energy conversion efficiency of a TE material is determined by a dimensionless figure of merit

$$zT = S^2\sigma T/k \quad (1)$$

where S, σ, κ, and T are the Seebeck coefficient (μV K^{-1}), electrical conductivity (S m^{-1}), thermal conductivity (W m^{-1} K^{-1}), and absolute temperature (K), respectively. κ includes the electronic thermal conductivity (κ_e) and lattice thermal conductivity (κ_L):

$$\kappa = \kappa_e + \kappa_L \quad (2)$$

Besides, $S^2\sigma$ is defined as the power factor (PF). A good TE material is thus characterized by high S and σ, and low κ values.

Silver selenide (Ag_2Se) is one of the very few TE materials suitable for use at ambient temperature, where it is characterized by relatively low thermal conductivity and high electrical conductivity.[5] Ag_2Se is an n-type semiconductor with a narrow band gap (E_g = 0.07 eV at 0 K). It exists in two stable phases, the low-temperature orthorhombic β-phase and the high-temperature cubic α-phase, with a transition temperature of around 407 K.[6−8] Numerous approaches exist for the synthesis of Ag_2Se. Among them, the commonly reported solid-state preparation strategy is based on reacting the two elements, Ag and Se, at high temperatures[6,9−15] or using high-energy ball milling.[8,16] As an example, Chen et al. developed a porous Ag_2Se with hierarchical structures via a wet mechanical alloying process. Using this approach, a low lattice thermal conductivity of ∼0.35 W m^{-1} K^{-1} and a zT of ∼0.7 were obtained at 300 K.[8] Besides, Ag_2Se is also produced by

Special Issue: Advanced Thermoelectric Materials and Devices

Received: January 13, 2023
Accepted: April 24, 2023

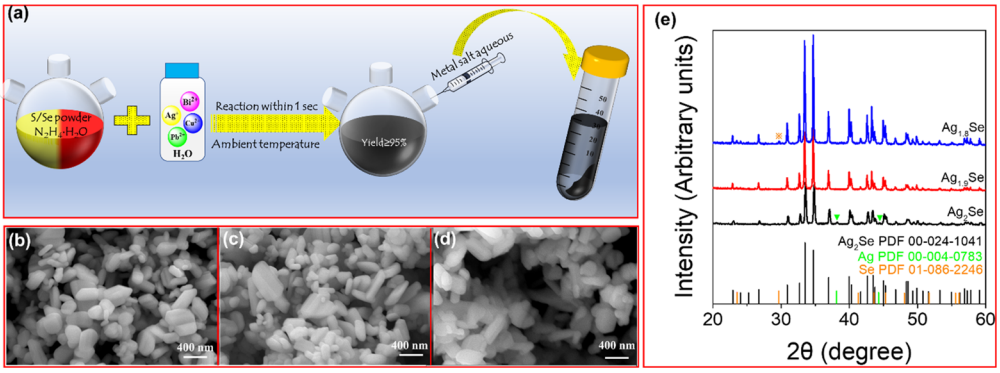

Figure 1. (a) Schematic illustration of the synthesis of binary metal chalcogenides (MX; M = Ag, Cu, Pb, Bi; X = S, Se). (b–d) SEM images of Ag_2Se produced from $AgNO_3$:Se molar ratios of (b) 2:1, (c) 1.9:1, and (d) 1.8:1. (e) XRD patterns of Ag_2Se.

vacuum-based technologies such as magnetron sputtering.[17] Various chemical synthetic methods have also been reported for the production of silver chalcogenides and particularly Ag_2Se particles, including colloidal,[18−21] hydrothermal,[22,23] and microwave-assisted[24] methods. In some cases, aqueous solutions have been used.[5,25,26] As an example, Xiao et al. synthesized Ag_2Se nanocrystals via a colloidal method, reaching a maximum zT value of 0.23 at the phase transition temperature of around 408 K.[19] Wang et al. reported a general aqueous synthesis of nano/microscale binary silver chalcogenides (Ag_2X, X = S, Se, Te) based on the reaction of Na_2S/NaHSe/NaHTe and $AgNO_3$ aqueous solution at the water boiling temperature. The molar ratios of Ag^+/X^{2-} were adjusted from 2:1 to 2:1.1 and the maximum zT value of the resulting Ag_2Se pellet was 0.84 at 380 K.[25]

The TE properties of pristine Ag_2Se can be improved through extrinsic and intrinsic doping. Li et al. reported a hydrothermal solution route using ethylene glycol and glycerol as solvents to prepare Ag_2Se at 180 °C, reaching a maximum zT of 0.7 at 317 K for Ag_2Se, and up to 0.9 at 300 K when adding 0.1 wt % Sn doping at Ag sites.[27] Variations in the stoichiometric ratio of silver to selenium were also investigated to control the concentration of free carriers, showing an obvious effect on the TE performance.[11,16,17] In this direction, Jood et al. introduced an anion excess (≤1% of Se or S) into Ag_2Se obtaining a notable improvement in carrier mobility and zT values up to ∼1.0 in the temperature range of 300−375 K.[13,14] Another important approach to improving Ag_2Se performance is to combine it with small amounts of other materials into nanocomposites.[28−31] As an example, Ballikaya et al. added Cu_2Se nanoinclusions in Ag_2Se to improve the TE performance and thermal stability.[32] Lim et al. obtained a high zT of 0.89 at 343 K through the simple blending of Ag_2Se with Te nanorods.[18] Besides, carbon nanotubes were also used as an effective nanofiller for enhancing the TE performance of Ag_2Se.[5,23]

Bismuth sulfide (Bi_2S_3) is an n-type semiconductor composed of relatively abundant, nontoxic, and low-cost elements.[33] Bi_2S_3 has poor zT values at ambient temperature, because of moderate electrical conductivity. However, it is characterized by high Seebeck coefficients (ca. −400 μV/K) and low thermal conductivities. Bi_2S_3 has been used as a doping phase to promote the TE properties of some TE materials, including $Cu_{1.8}S$[34] and $Bi_2Te_{2.7}Se_{0.3}$.[35]

Herein, we detail a facile, rapid, room temperature, and aqueous-based general approach to producing highly crystalline Ag_2Se. Besides, a series of Ag_2Se-x wt % Bi_2S_3 (x = 0, 0.5, 1.0 and 1.5) nanocomposites is produced by solution-blending and hot pressing. Interestingly, the incorporation of Bi_2S_3 results in a significant increase in the Seebeck coefficient. Furthermore, the optimized composition shows low thermal conductivity and a record-high zT of 0.96 at 370 K.

EXPERIMENTAL SECTION

Materials. Silver(I) nitrate ($AgNO_3$, 99.9+%), copper(II) nitrate trihydrate ($Cu(NO_3)_2·3H_2O$, 99%), lead(II) nitrate ($Pb(NO_3)_2$, 99+%), and hydrazine hydrate ($N_2H_4·H_2O$, 64%) were supplied by Fisher Scientific. Selenium powder (Se, 200 mesh, ≥ 99.5% trace metals basis), bismuth nitrate pentahydrate ($Bi(NO_3)_3·5H_2O$, ≥ 99.99%), thioacetamide (TAA, ≥ 99.0%), and nitric acid (HNO_3, 68%) were purchased from Sigma-Aldrich. All chemicals were used without further purification using standard solution synthesis procedures.[36,37]

Synthesis of Silver Selenide. In a typical synthetic method, 0.8494 g of $AgNO_3$ was dissolved into 10 mL of deionized water (DIW). In parallel, a Se precursor solution was prepared by adding 0.2078 g of Se powder to 5 mL of $N_2H_4·H_2O$. The $AgNO_3$ aqueous solution was then injected at ambient temperature into the Se solution, where a black precipitate was immediately formed. The product was collected by centrifugation and washed using DIW and ethanol three times. The final product was dried and stored in an Ar-filled glovebox.

Synthesis of Metal Chalcogenide (MX). For the production of other binary metal chalcogenides (MX, M = Cu, Pb, Bi; X = S, Se) a similar synthesis strategy was adopted. The detailed parameters are shown in Table S1. It is worth mentioning that SnS and SnSe can also be prepared by the same approach in an alkaline water environment (e.g., sodium hydroxide aqueous solution), but they require a longer reaction time (ca. 1 h) at ambient temperature.

Synthesis of Bismuth Sulfide. Bi_2S_3 was synthesized in an aqueous solution following an alternative procedure inspired by previous publications.[38,39] Briefly, TAA (0.510 g) was dissolved in 160 mL of DIW with rapid stirring. At the same time, $Bi(NO_3)_3·5H_2O$ (1.584 g) was added to 20 mL of 0.4 M HNO_3 aqueous solution, and then it was added drop by drop to the TAA solution. The mixture was reacted for 15 h at room temperature with continuous strong stirring. The coarse product solution was washed with DIW and ethanol five times. Finally, it was dried and stored in an Ar-filled glovebox.

Nanopowder Blend and Consolidation. Ag_2Se/Bi_2S_3 composite powders were produced by blending the proper ratio of particles of the two materials in solution under ultrasonication for 1 h. Next, the dried blended powders were placed in a furnace and annealed at 250 °C for 1 h in an Ar/H_2 flow. The annealed powders were loaded into a graphite die (Ø 10 mm × 10 mm cylinders) and hot-pressed for 5 min at 50 MPa and 250 °C inside an argon-filled glovebox. The hot-pressed pellets were then polished and used for TE characterization.

https://doi.org/10.1021/acsaelm.3c00055
ACS Appl. Electron. Mater. XXXX, XXX, XXX−XXX

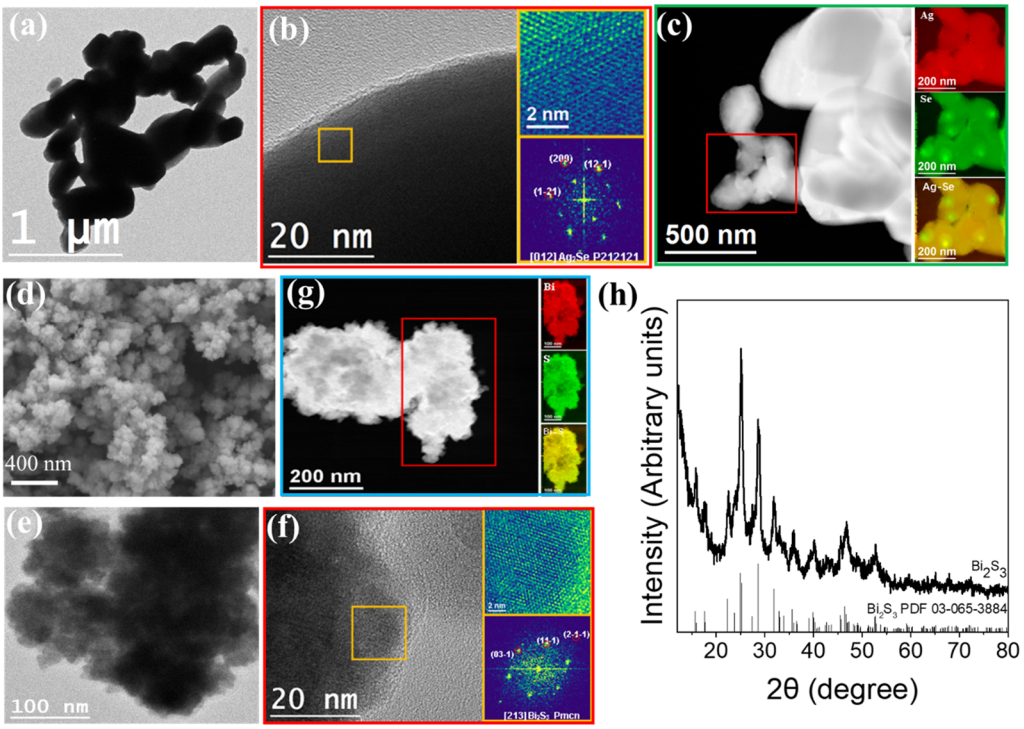

Figure 2. Structural and Chemical Characterization of Ag_2Se and Bi_2S_3. (a) TEM micrograph of Ag_2Se. (b) HRTEM micrograph of Ag_2Se, detail of the orange squared region, and its corresponding power spectrum. (c) EELS chemical composition maps from the red square area of the STEM micrograph of Ag_2Se. Individual Ag M4,5-edges at 367 eV (red), Se M1-edges at 232 eV (green), and composites of Ag−Se. (d) SEM image of Bi_2S_3. (e) TEM and (f) HRTEM micrograph of Bi_2S_3, detail of the orange square region, and its corresponding power spectrum. From the crystalline domain, the Bi_2S_3 lattice fringe distances were measured to be 0.351 0.354, and 0.193 nm, at 66.70° and 96.72°, which could be interpreted as the orthorhombic Bi_2S_3 phase visualized along its [213] zone axis. (g) EELS chemical composition maps from the red square area of the STEM micrograph of Bi_2S_3. Individual Bi N4,5-edges at 440 eV (red), S L2,3-edges at 165 eV (green), and composites of Bi−S. (h) XRD pattern of Bi_2S_3.

RESULTS AND DISCUSSION

Figure 1a shows a schematic illustration of the aqueous and ambient temperature synthesis process used to produce binary metal chalcogenides (MX; M = Ag, Cu, Pb, Bi; X = S, Se). The MX chalcogenide is produced by the reaction of the zerovalent chalcogen (X^0) powder with $N_2H_4{\cdot}H_2O$ to form X^{2-} and the immediate reaction of such anions with the metal cations in the metal salt solution. In this way, Ag_2S, Ag_2Se, CuS, Cu_2S, Cu_2Se, Bi_2S_3, Bi_2Se_3, PbS, and PbSe particles, which through proper processing can be used in a plethora of different applications,[40−48] were easily and rapidly obtained. Figure 1b−d displays scanning electron microscopy (SEM) images of Ag_2Se produced from different $AgNO_3$:Se molar ratios; 2:1, 1.9:1, and 1.8:1. Ag_2Se particles are characterized by elongated shapes, an average size of a few hundred nanometers, and high crystallinity, as observed by X-ray diffraction (XRD, Figure 1e). XRD patterns show the obtained Ag_2Se to have an orthorhombic crystallographic phase (PDF 00−024−1041) with lattice parameters a = 4.333 Å, b = 7.062 Å, and c = 7.764 Å. At an $AgNO_3$:Se molar ratio of 2:1, a few impurity peaks at 38.2° and 44.3° can be indexed with the cubic Ag phase (PDF 00−004−0783). At a $AgNO_3$/Se molar ratio of 1.8:1, a new peak at 29.6° is ascribed to the hexagonal Se phase (PDF 01−086−2246), indicating that the excess Se was not fully incorporated into the Ag_2Se lattice. At a $AgNO_3$:Se molar ratio of 1.9:1, XRD patterns show pure-phase Ag_2Se, with no crystalline impurities. Thus, we chose this precursor molar ratio to prepare the material to be further characterized and used to produce Ag_2Se/Bi_2S_3 composites. At this $AgNO_3$:Se molar ratio of 1.9:1, energy-dispersive X-ray spectroscopy (EDX) analysis shows the Ag:Se atomic ratio in the final Ag_2Se particles to be 2.2 (Figure S1). However, for the sake of convenience, we denote the silver selenide as Ag_2Se. The SEM images, To demonstrate the versatility of the synthesis approach here reported, EDX data and XRD patterns of other MX (M = Ag, Cu, Pb, and Bi, X = S and Se) are displayed in Figure S2, Table S2, and Figure S3, respectively.

Figure 2a shows a general view bright field transmission electron microscopy (TEM) image of produced Ag_2Se. Figure 2b shows a high-resolution HRTEM micrograph from an Ag_2Se particle and its corresponding power spectrum revealing an orthorhombic crystal phase (space group $P2_12_12_1$) with a = 4.334 Å, b = 7.070 Å, c = 7.774 Å. The high-angle annular dark field (HAADF) scanning TEM (STEM) micrographs and electron energy loss spectroscopy (EELS) composition maps of Ag_2Se particles show a homogeneous distribution of both elements (Figure 2c).

Bi_2S_3 particles were also synthesized in an aqueous solution at ambient temperature. Figure 2d,e shows representative SEM and TEM images of the obtained product. Bi_2S_3 particles were highly polycrystalline and presented a flowerlike morphology. Crystallites had an average size of ca. 10 nm. EDX analysis showed the atomic ratio of Bi to S to be consistent with stoichiometric Bi_2S_3. HRTEM analysis showed the particle crystal structure to agree with the Bi_2S_3 orthorhombic phase (space group = *Pmcn*) with a = 3.9810 Å, b = 11.1470 Å, and c = 11.3050 Å (Figure 2f). EELS compositional maps showed a homogeneous distribution of Bi and S (Figure 2g). Besides,

https://doi.org/10.1021/acsaelm.3c00055
ACS Appl. Electron. Mater. XXXX, XXX, XXX−XXX

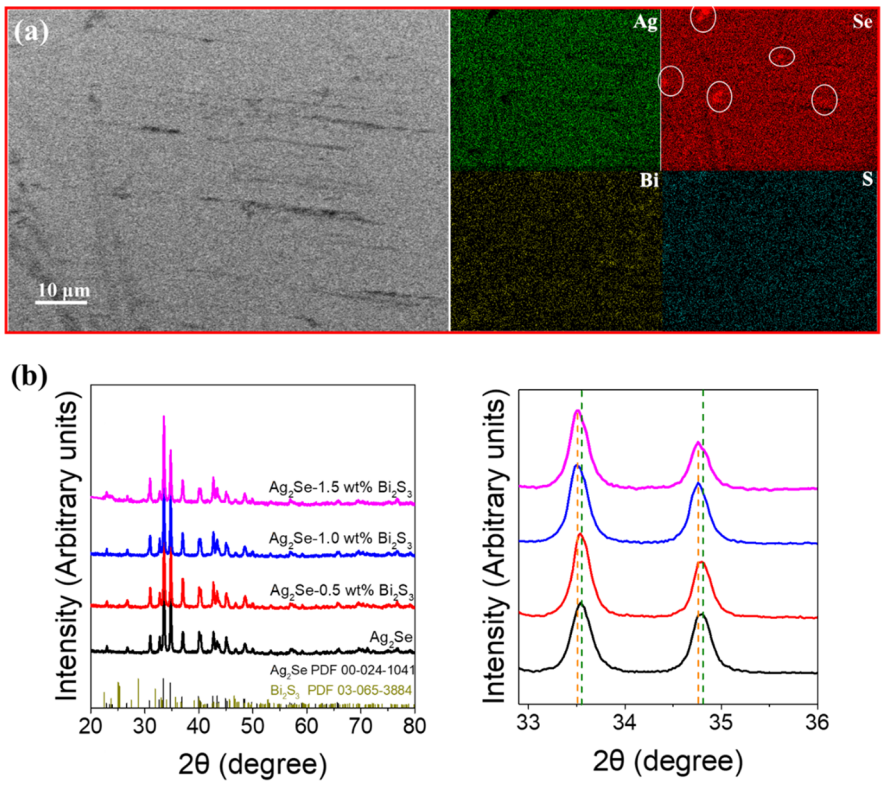

Figure 3. (a) SEM image of the polished Ag_2Se-1.0 wt % Bi_2S_3 pellet and corresponding EDX compositional maps of Ag, Se, Bi, and S (Se-rich regions marked with white circles). (b) XRD patterns of consolidated Ag_2Se-*x* wt % Bi_2S_3 pellets.

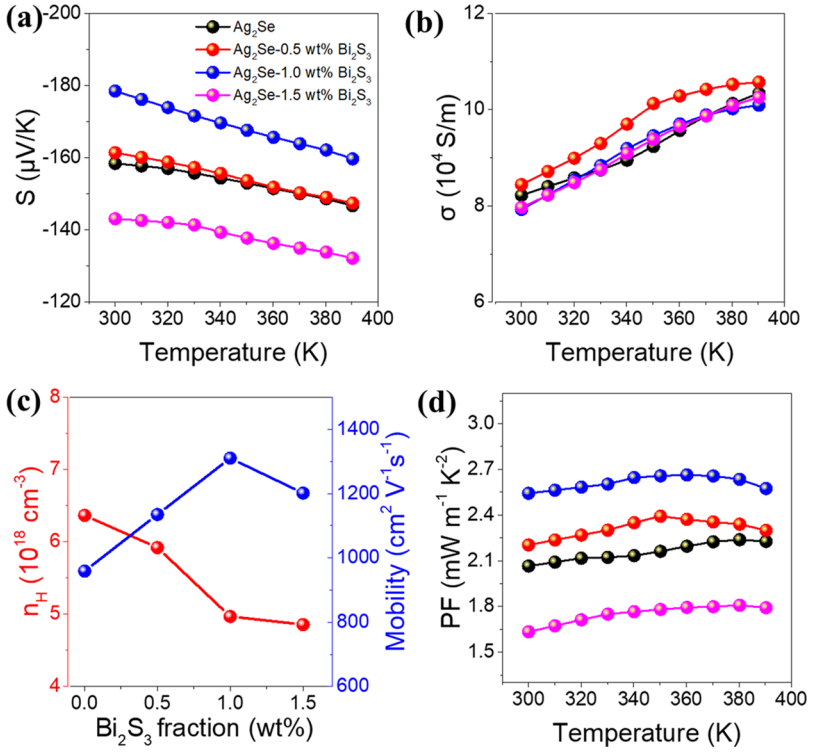

Figure 4. Temperature dependence of (a) Seebeck coefficient and *S*. (b) electrical conductivity, σ. (c) Hall carrier concentration (n_H) and mobility (μ_H) at room temperature. (d) Power factor PF of Ag_2Se-*x* wt % Bi_2S_3.

XRD data confirmed the orthorhombic phase (PDF 03−065−3884) of the Bi_2S_3 particles (Figure 2h).

Ag_2Se/Bi_2S_3 composites were produced by blending the proper ratio of particles in solution and hot pressing the resulting dried powder at 50 MPa and 250 °C inside an argon-filled glovebox (see the Experimental section for details). An SEM image of the polished surface of the Ag_2Se-1.0 wt % Bi_2S_3 composite and its corresponding EDX elemental maps are

https://doi.org/10.1021/acsaelm.3c00055
ACS Appl. Electron. Mater. XXXX, XXX, XXX−XXX

shown in Figure 3a. Besides, the morphology of a fractured Ag_2Se-1.0 wt % Bi_2S_3 sample and its compositional map and EDX compositions of all fractured pellets are shown in Figure S4 and Table S3. An overall homogeneous distribution of the constituent elements, including S and Bi, is observed, denoting atomic doping of the Ag_2Se with these two elements. Only some small Se-rich inhomogeneities can be found, as marked with white circles. Figure 3b shows the XRD patterns of the hot-pressed Ag_2Se-x wt % Bi_2S_3 composites, which can be indexed with the orthorhombic Ag_2Se phase (PDF 00−024−1041). As the Bi_2S_3 content increases, the XRD peaks shift slightly to lower angles, indicating an expansion of the lattice associated with the partial substitution of Ag^+ ions (0.67 Å) by Bi^{3+} ions (1.03 Å) with a larger ionic radius.[49] However, when the Bi_2S_3 content exceeds 1.0 wt %, the XRD peaks no longer shift due to the limited solubility of Bi^{3+} in the matrix. No impurity XRD peaks and particularly Bi_2S_3 peaks were detected, indicating notable alloying of Bi_2S_3 with Ag_2Se.[34] The density of the composite slightly decreases with the increase of the Bi_2S_3 fraction due to the lower density of Bi_2S_3 (~6.78 g/cm^3) compared with Ag_2Se[35] but all samples reach relative densities above 90% (Table S4).

The temperature dependence of the Seebeck coefficient (S) of the different composites is shown in Figure 4a. All samples show n-type semiconducting behavior with negative S values. The absolute values of S monotonously decrease with temperature over the entire measured range. The S of the pure Ag_2Se sample reaches up to −158.4 μV/K at 300 K and decreases to −146.7 μV/K at 390 K. With the introduction of Bi_2S_3, the absolute S values increased significantly reaching up to −178.5 μV/K at 300 K for the Ag_2Se-1.0 wt % Bi_2S_3 pellet.

As displayed in Figure 4b, the temperature dependence of the electrical conductivity (σ) of the different composites shows a typical nondegenerate semiconductor characteristic with σ monotonously increasing with temperature. Relatively similar σ values were obtained for the different doping composites.

The charge carrier concentration (n_H) and mobility (μ_H) as a function of the Bi_2S_3 amount were measured by Hall and are displayed in Figure 4c. As the concentration of Bi_2S_3 increases, the n_H for Ag_2Se-x wt % Bi_2S_3 exhibits a moderate decrease (6.4×10^{18} cm^{-3} for pure Ag_2Se and 4.9×10^{18} cm^{-3} for Ag_2Se-1.5 wt % Bi_2S_3). In contrast, the μ_H for Ag_2Se-x wt % Bi_2S_3 samples first rises and then decreases gradually with rising Bi_2S_3 concentration. In detail, the μ_H is 958.9 cm^2 V^{-1} s^{-1} for the pure Ag_2Se sample, and the largest value of 1310.4 cm^2 V^{-1} s^{-1} is found as Bi_2S_3 amount increases to 1.0 wt %. A further increase of Bi_2S_3 doping concentration to 1.5 wt % reduces the μ_H of Ag_2Se-x wt % Bi_2S_3 samples.

The increase in the absolute value of the Seebeck coefficient with the introduction of Bi_2S_3 is in part associated with the decrease in the charge carrier concentration. Previous studies also demonstrate an increase in the absolute value of the Seebeck coefficient and also the charge carrier mobility with the partial replacement of Se with S.[13,50] Besides, the Bi doping within the Ag_2Se lattice expands the lattice, as observed by XRD, which according to previous publications could increase the density of states near the Fermi level,[51−53] thereby further enhancing the Seebeck coefficient of the Ag_2Se-based materials. At too high, Bi_2S_3 precipitates are found as a secondary phase inside the Ag_2Se matrix, which reduces the charge carrier mobility and the absolute value of the Seebeck coefficient. This reduction may be related to a higher bipolar contribution associated with the preferential scattering of electrons over holes at the Ag_2Se/Bi_2S_3 interphase owing to the upward band bending generated at the Ag_2Se side. It is therefore crucial to maintain the Bi_2S_3 content below 1% to achieve an optimal thermoelectric performance in $Ag_2Se−Bi_2S_3$ composites. Notice that a similar evolution of the Seebeck coefficient with dopant concentration, first increasing and later decreasing at higher dopant concentrations, has been reported in other systems, and diverse mechanisms have been reported.[54−57] Besides, previous studies have also shown increased Seebeck coefficients without affecting the electrical conductivity.[58−60] The preserved electrical conductivity of Ag_2Se after being mixed with Bi_2S_3 is attributed to the notable increase in charge carrier mobility, which compensates for the moderate decrease in charge carrier concentration.

Figure 4d shows the power factor (PF, $S^2\sigma$) of Ag_2Se-x wt % Bi_2S_3 samples as a function of temperature. For the pure Ag_2Se sample, the PF slightly increases, from 2.06 to 2.24 mW m^{-1} K^{-2} over 300−390 K. The PF of the Ag_2Se −1.0 wt % Bi_2S_3 composite is significantly larger, reaching up to 2.66 mW m^{-1} K^{-2} at 360 K. Notice also that the Ag_2Se-1.0 wt % Bi_2S_3 pellet exhibits good stability even after multiple tests (Figure S5).

The experimental thermal diffusivities, α, are presented in Table S4. The measured heat capacities, C_p, and the limit C_p calculated by the Dulong−Petit law are shown in Figure S6. Notice that while the measured C_p is very close to the calculated limit for the Ag_2Se-x wt % Bi_2S_3 composite and slightly below this limit for the pure Ag_2Se sample, the limit is approximately within the error range of the measured values.[61,62] The total thermal conductivity (κ_{tot}) is determined by the equation

$$\kappa_{tot} = \alpha\rho C_p \quad (3)$$

where ρ is density. Figure 5a displays the obtained thermal conductivity of Ag_2Se and Ag_2Se-x wt % Bi_2S_3 samples over the

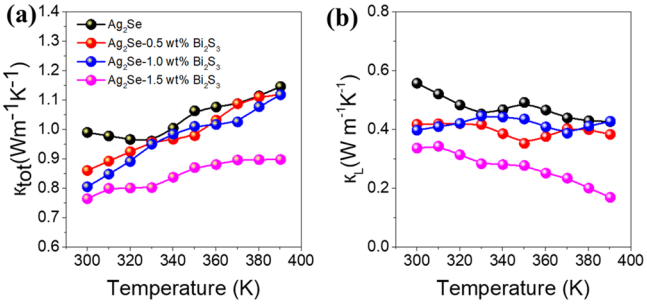

Figure 5. Thermal conductivity of (a) total thermal conductivity, κ_{tot}. (b) Lattice thermal conductivity κ_L.

whole temperature range. The pure Ag_2Se pellet is characterized by a moderate κ_{tot} of 0.99 W m^{-1} K^{-1} at 300 K and 1.15 W m^{-1} K^{-1} at 390 K. These values are consistent with previous reports on Ag_2Se.[25] With the introduction of Bi_2S_3, κ_{tot} significantly decreases. The Ag_2Se-1.5 wt % Bi_2S_3 sample displayed the lowest κ_{tot}, 0.76 W m^{-1} K^{-1} at 300 K and 0.90 W m^{-1} K^{-1} at 390 K. Figure 5b displays the lattice thermal conductivity (κ_L) obtained by subtracting the electronic contribution to the thermal conductivity calculated using a single parabolic band (SPB) model according to Wiedemann−Franz ($\kappa_e = L\sigma T$, where L is the Lorentz number) from the total thermal conductivity ($\kappa_L = \kappa_{tot} - \kappa_e$). The Lorenz number L is calculated by

https://doi.org/10.1021/acsaelm.3c00055
ACS Appl. Electron. Mater. XXXX, XXX, XXX−XXX

$$L = 1.5 + \exp\left[-\frac{|S|}{116}\right] \quad (4)$$

The plot is displayed in Figure S7a. Figure S7b shows the temperature dependence of κ_e. While similar κ_e values were obtained for the different materials, composites displayed lower κ_L, down to 0.34−0.17 W m^{-1} K^{-1} for Ag_2Se-1.5 wt % Bi_2S_3. The lower κ_{tot} measured for the composites is associated with a more effective scattering of phonons at point defects created by Bi^{3+} and extensive interphases between Ag_2Se and Bi_2S_3 in the case of the highest doped samples. Numerous previous works have reported a decrease of thermal conductivity with a minor effect on electrical conductivity and have associated this phenomenon with different explanations, including a strong scattering on phonons created by precipitates without strongly affecting electrical conductivity,[63] hierarchical architecture with multiscale defects differently affecting phonons and electrons,[60] phonon scattering by introduced electrically dopant atoms,[64] and preferential phonon scattering by introduced nanoparticles.[65]

The temperature dependence of the TE figure or merit, zT, is displayed in Figure 6a. For the pristine Ag_2Se pellet, the zT value increases from 0.62 at 300 K to 0.76 at 380 K. The zT values of the Ag_2Se-x wt % Bi_2S_3 composites increase with the introduction of 0.5−1.0 wt % Bi_2S_3. A maximum zT value of 0.96 was obtained for the Ag_2Se-1.0 wt % Bi_2S_3 sample at 370 K, which is ascribed to the highest PF value and slightly decreased κ_{tot}. These zT values are above those previously reported n-type Ag_2Se -based TE materials prepared by wet chemistry[18,19,22,23,25,27,66] and other methods[15,32,67,68] (Figure 5b and Table S5). We further determined the thermoelectric properties of a pure Ag_2Se sample up to 480 K (Figure S8). We noticed that above 400 K, coinciding with the Ag_2Se phase transition, a large decrease in the absolute value of the Seebeck coefficient and electrical conductivity was obtained, which resulted in an abrupt drop of zT. Thus, the material application is limited to a temperature range extending up to about 390 K.

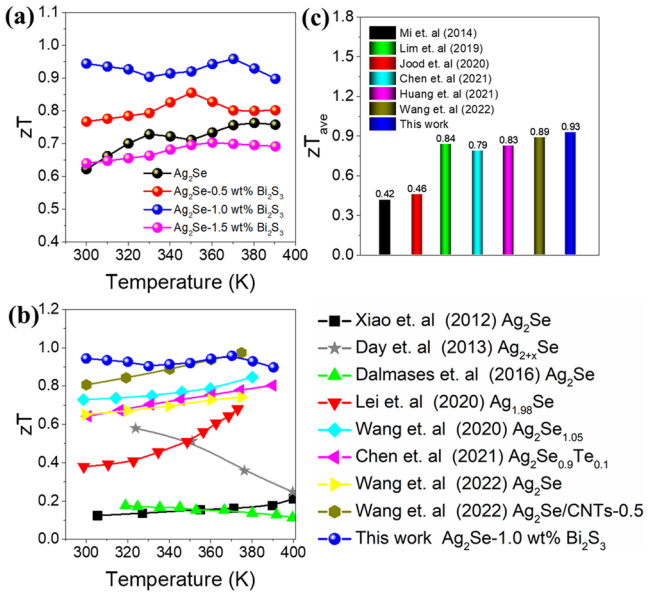

Figure 6. Temperature dependence of (a) zT values of Ag_2Se-x wt % Bi_2S_3, (b) a comparison with reported silver selenide-based thermoelectric materials,[5,10,19,25,66,69,70] and (c) a comparison of zT_{ave} with reported data of silver selenide-based thermoelectric materials.[5,11,13,15,18,68]

zT values remain constant throughout the whole temperature range tested, providing a high average zT (zT_{ave}) calculated as

$$zT_{ave} = \frac{1}{T_h - T_c}\int_{T_c}^{T_h} zT\,dT \quad (5)$$

where T_h is the hot-side temperature, T_c is the cold-side temperature, and zT_{ave} is thus the area under the zT curve divided by the value of $T_h - T_c$. As shown in Figure 6c, a zT_{ave} = 0.93 is obtained in the temperature range of 300 to 390 K for the Ag_2Se-1.0 wt % Bi_2S_3 sample, significantly above previously reported values.

CONCLUSIONS

In conclusion, a facile, rapid, high-yield, and component-controllable room-temperature aqueous synthesis method was adopted to prepare a plethora of metal chalcogenide MX nanoparticles (M = Ag, Cu, Pb, Bi; X = S, Se). Using this procedure, a series of Ag_2Se-x wt % Bi_2S_3 composites was obtained by blending the materials in solution and hot press sintering the obtained dried powder. A maximum zT value of 0.76 for pure Ag_2Se was obtained at 380 K. Further investigation illustrates that moderate Bi_2S_3 doping can effectively increase the absolute S value and reduce κ_L without significant harm to σ, which contributes to a remarkable PF of 2.66 mW m^{-1} K^{-2} and a maximum zT of 0.96 at 370 K. Besides, a remarkable zT_{ave} of 0.93 was obtained for Ag_2Se-1.0 wt % Bi_2S_3 nanocomposites, above the values obtained in most previous silver selenide-based thermoelectric materials fabricated via wet chemical approaches.

ASSOCIATED CONTENT

Supporting Information

The Supporting Information is available free of charge at https://pubs.acs.org/doi/10.1021/acsaelm.3c00055.

Experimental characterization details, additional SEM, XRD, EDX data, reproducibility results, heat capacities, calculation of the Lorenz number, and comparison with previous literature (PDF)

AUTHOR INFORMATION

Corresponding Authors

Yu Zhang − *Department of Materials Science and Engineering, Pennsylvania State University, State College, Pennsylvania 16802, United Sates*; Email: yvz5897@psu.edu

Andreu Cabot − *Catalonia Institute for Energy Research−IREC, Sant Adrià del Besòs 08930, Spain; ICREA, Barcelona 08010 Catalonia, Spain*; orcid.org/0000-0002-7533-3251; Email: acabot@irec.cat

Authors

Bingfei Nan − *Catalonia Institute for Energy Research−IREC, Sant Adrià del Besòs 08930, Spain; Departament d'Enginyeria Electrònica i Biomèdica, Universitat de Barcelona, Barcelona 08028 Catalonia, Spain*

Mengyao Li − *Catalonia Institute for Energy Research−IREC, Sant Adrià del Besòs 08930, Spain; School of Physics and Microelectronics, Zhengzhou University, Zhengzhou 450052, China*; orcid.org/0000-0002-9082-7938

https://doi.org/10.1021/acsaelm.3c00055
ACS Appl. Electron. Mater. XXXX, XXX, XXX−XXX

Ke Xiao − *Catalonia Institute for Energy Research−IREC, Sant Adrià del Besòs 08930, Spain; Departament d'Enginyeria Electrònica i Biomèdica, Universitat de Barcelona, Barcelona 08028 Catalonia, Spain*
Khak Ho Lim − *Institute of Zhejiang University−Quzhou, Quzhou 324000 Zhejiang, P.R. China; College of Chemical and Biological Engineering, Zhejiang University, Hangzhou 310007 Zhejiang, P.R. China*
Cheng Chang − *Institute of Science and Technology Austria (ISTA), Klosterneuburg 3400, Austria; School of Materials Science and Engineering, Beihang University, Beijing 100191, China*
Xu Han − *Catalan Institute of Nanoscience and Nanotechnology (ICN2), Barcelona 08193 Catalonia, Spain*
Yong Zuo − *Istituto Italiano di Tecnologia, Genova 16163, Italy*
Junshan Li − *Institute for Advanced Study, Chengdu University, Chengdu 610106, China*
Jordi Arbiol − *Catalan Institute of Nanoscience and Nanotechnology (ICN2), Barcelona 08193 Catalonia, Spain; ICREA, Barcelona 08010 Catalonia, Spain;* orcid.org/0000-0002-0695-1726
Jordi Llorca − *Institute of Energy Technologies, Department of Chemical Engineering and Barcelona Research Center in Multiscale Science and Engineering, Barcelona East School of Engineering, Universitat Politècnica de Catalunya, Barcelona 08019 Catalonia, Spain;* orcid.org/0000-0002-7447-9582
Maria Ibáñez − *Institute of Science and Technology Austria (ISTA), Klosterneuburg 3400, Austria;* orcid.org/0000-0001-5013-2843

Complete contact information is available at: https://pubs.acs.org/10.1021/acsaelm.3c00055

Funding

Open Access is funded by the Austrian Science Fund (FWF).

Notes

The authors declare no competing financial interest.

■ ACKNOWLEDGMENTS

B.N., M.L., Y.Z., K.X., and X.H. thank the China Scholarship Council (CSC) for the scholarship support. C.C. received funding from the FWF "Lise Meitner Fellowship" grant agreement M 2889-N. M.I. acknowledges the financial support from ISTA and the Werner Siemens Foundation. ICN2 acknowledges funding from Generalitat de Catalunya 2021SGR00457 and project NANOGEN (PID2020-116093RB-C43) funded by MCIN/AEI/10.13039/501100011033/. ICN2 was supported by the Severo Ochoa program from Spanish MCIN/AEI (Grant No.: CEX2021-001214-S) and was funded by the CERCA Programme/Generalitat de Catalunya. J.L. is a Serra Húnter Fellow and is grateful to the ICREA Academia program and projects MICINN/FEDER PID2021-124572OB-C31 and 2021 SGR 01061. K.H.L. acknowledges support from the National Natural Science Foundation of China (22208293). This study is part of the Advanced Materials programme and was supported by MCIN with funding from European Union NextGenerationEU (PRTR-C17.I1) and by Generalitat de Catalunya.

■ REFERENCES

(1) Liu, W.-D.; Shi, X.-L.; Moshwan, R.; Yang, L.; Chen, Z.-G.; Zou, J. Solvothermal synthesis of high-purity porous $Cu_{1.7}Se$ approaching low lattice thermal conductivity. *Chem. Eng. J.* **2019**, *375*, 121996.
(2) He, J.; Tritt, T. M. Advances in thermoelectric materials research: Looking back and moving forward. *Science* **2017**, *357*, 9.
(3) Shi, X.-L.; Zou, J.; Chen, Z.-G. Advanced Thermoelectric Design: From Materials and Structures to Devices. *Chem. Rev.* **2020**, *120*, 7399−7515.
(4) Zhang, Y.; Li, Z.; Singh, S.; Nozariasbmarz, A.; Li, W.; Genç, A.; Xia, Y.; Zheng, L.; Lee, S. H.; Karan, S. K.; et al. Defect Engineering Stabilized $AgSbTe_2$ with High Thermoelectric Performance. *Adv. Mater.* **2023**, *35*, 2208994.
(5) Wang, H. T.; Ma, H. Q.; Duan, B.; Geng, H. Y.; Zhou, L.; Li, J. L.; Zhang, X. L.; Yang, H. J.; Li, G. D.; Zhai, P. C. High-Pressure Rapid Preparation of High-Performance Binary Silver Sulfide Thermoelectric Materials. *ACS Appl. Energy Mater.* **2021**, *4*, 1610−1618.
(6) Ferhat, M.; Nagao, J. Thermoelectric and transport properties of β-Ag_2Se compounds. *J. Appl. Phys.* **2000**, *88*, 813−816.
(7) Dalven, R.; Gill, R. Energy Gap in β−Ag_2Se. *Phys. Rev.* **1967**, *159*, 645−649.
(8) Chen, J.; Sun, Q.; Bao, D.; Liu, T.; Liu, W.-D.; Liu, C.; Tang, J.; Zhou, D.; Yang, L.; Chen, Z.-G. Hierarchical Structures Advance Thermoelectric Properties of Porous n-type β-Ag_2Se. *ACS Appl. Mater. Interfaces* **2020**, *12*, 51523−51529.
(9) Conn, J. B.; Taylor, R. C. Thermoelectric and Crystallographic Properties of Ag_2Se. *J. Electrochem. Soc.* **1960**, *107*, 977.
(10) Day, T.; Drymiotis, F.; Zhang, T.; Rhodes, D.; Shi, X.; Chen, L.; Snyder, G. J. Evaluating the potential for high thermoelectric efficiency of silver selenide. *J. Mater. Chem. C* **2013**, *1*, 7568−7573.
(11) Mi, W.; Qiu, P.; Zhang, T.; Lv, Y.; Shi, X.; Chen, L. Thermoelectric transport of Se-rich Ag_2Se in normal phases and phase transitions. *Appl. Phys. Lett.* **2014**, *104*, 133903.
(12) Ahmad, S.; Singh, A.; Bhattacharya, S.; Basu, R.; Bhatt, R.; Muthe, K. P. Near room temperature thermoelectrics: Ag_2Se. *J. Appl. Phys.* **2020**, *2265*, No. 030429.
(13) Jood, P.; Chetty, R.; Ohta, M. Structural stability enables high thermoelectric performance in room temperature Ag_2Se. *J. Mater. Chem. A* **2020**, *8*, 13024−13037.
(14) Jood, P.; Ohta, M. Temperature-Dependent Structural Variation and Cu Substitution in Thermoelectric Silver Selenide. *ACS Appl. Energy Mater.* **2020**, *3*, 2160−2167.
(15) Huang, S.; Wei, T.-R.; Chen, H.; Xiao, J.; Zhu, M.; Zhao, K.; Shi, X. Thermoelectric Ag_2Se: Imperfection, Homogeneity, and Reproducibility. *ACS Appl. Mater. Interfaces* **2021**, *13*, 60192−60199.
(16) Lee, C.; Park, Y.-H.; Hashimoto, H. Effect of nonstoichiometry on the thermoelectric properties of a Ag_2Se alloy prepared by a mechanical alloying process. *J. Appl. Phys.* **2007**, *101*, No. 024920.
(17) Perez-Taborda, J. A.; Caballero-Calero, O.; Vera-Londono, L.; Briones, F.; Martin-Gonzalez, M. High Thermoelectric zT in n-Type Silver Selenide films at Room Temperature. *Adv. Energy Mater.* **2018**, *8*, 1702024.
(18) Lim, K. H.; Wong, K. W.; Liu, Y.; Zhang, Y.; Cadavid, D.; Cabot, A.; Ng, K. M. Critical role of nanoinclusions in silver selenide nanocomposites as a promising room temperature thermoelectric material. *J. Mater. Chem. C* **2019**, *7*, 2646−2652.
(19) Xiao, C.; Xu, J.; Li, K.; Feng, J.; Yang, J.; Xie, Y. Superionic Phase Transition in Silver Chalcogenide Nanocrystals Realizing Optimized Thermoelectric Performance. *J. Am. Chem. Soc.* **2012**, *134*, 4287−4293.
(20) Liu, Y.; Cadavid, D.; Ibáñez, M.; De Roo, J.; Ortega, S.; Dobrozhan, O.; Kovalenko, M. V.; Cabot, A. Colloidal $AgSbSe_2$ nanocrystals: surface analysis, electronic doping and processing into thermoelectric nanomaterials. *J. Mater. Chem. C* **2016**, *4*, 4756−4762.
(21) Cadavid, D.; Ibáñez, M.; Shavel, A.; Durá, O. J.; López de la Torre, M. A.; Cabot, A. Organic ligand displacement by metal salts to enhance nanoparticle functionality: thermoelectric properties of Ag_2Te. *J. Mater. Chem. A* **2013**, *1*, 4864−4870.

(22) Wang, H.; Chu, W.; Wang, D.; Mao, W.; Pan, W.; Guo, Y.; Xiong, Y.; Jin, H. Low-Temperature Thermoelectric Properties of β-Ag_2Se Synthesized by Hydrothermal Reaction. *J. Electron. Mater.* **2011**, *40*, 624−628.
(23) Chen, N.; Ren, C.; Sun, L.; Xue, H.; Yang, H.; An, X.; Yang, X.; Zhang, J.; Che, P. Improved thermoelectric properties of multi-walled carbon nanotubes/Ag_2Se via controlling the composite ratio. *CrystEngComm* **2022**, *24*, 260−268.
(24) Pei, J.; Chen, G.; Jia, D.; Jin, R.; Xu, H.; Chen, D. Rapid synthesis of Ag_2Se dendrites with enhanced electrical performance by microwave-assisted solution method. *New J. Chem.* **2013**, *37*, 323−328.
(25) Wang, H.; Liu, X.; Zhang, B.; Huang, L.; Yang, M.; Zhang, X.; Zhang, H.; Wang, G.; Zhou, X.; Han, G. General surfactant-free synthesis of binary silver chalcogenides with tuneable thermoelectric properties. *Chem. Eng. J.* **2020**, *393*, 124763.
(26) Tee, S. Y.; Tan, X. Y.; Wang, X.; Lee, C. J. J.; Win, K. Y.; Ni, X. P.; Teo, S. L.; Seng, D. H. L.; Tanaka, Y.; Han, M.-Y. Aqueous Synthesis, Doping, and Processing of n-Type Ag_2Se for High Thermoelectric Performance at Near-Room-Temperature. *Inorg. Chem.* **2022**, *61*, 6451−6458.
(27) Li, D.; Zhang, J. H.; Li, J. M.; Zhang, J.; Qin, X. Y. High thermoelectric performance for an Ag_2Se-based material prepared by a wet chemical method. *Mater. Chem. Front.* **2020**, *4*, 875−880.
(28) Zhang, Q.; Wu, G.; Guo, Z.; Sun, P.; Wang, R.; Chen, L.; Wang, X.; Tan, X.; Hu, H.; Yu, B.; Noudem, J. G.; Liu, G.; Jiang, J. Enhanced Thermoelectric and Mechanical Performances in Sintered $Bi_{0.48}Sb_{1.52}Te_3$−$AgSbSe_2$ Composite. *ACS Appl. Mater. Interfaces* **2021**, *13*, 24937−24944.
(29) Liu, H.-T.; Sun, Q.; Zhong, Y.; Deng, Q.; Gan, L.; Lv, F.-L.; Shi, X.-L.; Chen, Z.-G.; Ang, R. High-performance in n-type PbTe-based thermoelectric materials achieved by synergistically dynamic doping and energy filtering. *Nano Energy* **2022**, *91*, 106706.
(30) Chen, Y.; Chen, J.; Zhang, B.; Yang, M.; Liu, X.; Wang, H.; Yang, L.; Wang, G.; Han, G.; Zhou, X. Realizing enhanced thermoelectric properties in Cu_2S-alloyed SnSe based composites produced via solution synthesis and sintering. *J. Mater. Sci. Technol.* **2021**, *78*, 121−130.
(31) Zhang, Y.; Xing, C.; Liu, Y.; Li, M.; Xiao, K.; Guardia, P.; Lee, S.; Han, X.; Ostovari Moghaddam, A.; Josep Roa, J.; Arbiol, J.; Ibáñez, M.; Pan, K.; Prato, M.; Xie, Y.; Cabot, A. Influence of copper telluride nanodomains on the transport properties of n-type bismuth telluride. *Chem. Eng. J.* **2021**, *418*, 129374.
(32) Ballikaya, S.; Oner, Y.; Temel, T.; Ozkal, B.; Bailey, T. P.; Toprak, M. S.; Uher, C. Thermoelectric and thermal stability improvements in Nano-Cu_2Se included Ag_2Se. *J. Solid State Chem.* **2019**, *273*, 122−127.
(33) Ji, W.; Shi, X.-L.; Liu, W.-D.; Yuan, H.; Zheng, K.; Wan, B.; Shen, W.; Zhang, Z.; Fang, C.; Wang, Q.; Chen, L.; Zhang, Y.; Jia, X.; Chen, Z.-G. Boosting the thermoelectric performance of n-type Bi_2S_3 by hierarchical structure manipulation and carrier density optimization. *Nano Energy* **2021**, *87*, 106171.
(34) Zhang, Y.-X.; Ge, Z.-H.; Feng, J. Enhanced thermoelectric properties of $Cu_{1.8}S$ via introducing Bi_2S_3 and Bi_2S_3@Bi core-shell nanorods. *J. Alloy. Comp.* **2017**, *727*, 1076−1082.
(35) Zhu, Y.-K.; Guo, J.; Zhang, Y.-X.; Cai, J.-F.; Chen, L.; Liang, H.; Gu, S.-W.; Feng, J.; Ge, Z.-H. Ultralow Lattice Thermal Conductivity and Enhanced Power Generation Efficiency Realized in $Bi_2Te_{2.7}Se_{0.3}$/Bi_2S_3 nanocomposites. *Acta Mater.* **2021**, *218*, 117230.
(36) He, R.; Yang, L.; Zhang, Y.; Wang, X.; Lee, S.; Zhang, T.; Li, L.; Liang, Z.; Chen, J.; Li, J.; Ostovari Moghaddam, A.; Llorca, J.; Ibáñez, M.; Arbiol, J.; Xu, Y.; Cabot, A. A CrMnFeCoNi high entropy alloy boosting oxygen evolution/reduction reactions and zinc-air battery performance. *Energy Stor. Mater.* **2023**, *58*, 287−298.
(37) Montaña-Mora, G.; Qi, X.; Wang, X.; Chacón-Borrero, J.; Martinez-Alanis, P. R.; Yu, X.; Li, J.; Xue, Q.; Arbiol, J.; Ibáñez, M.; Cabot, A. Phosphorous incorporation into palladium tin nanoparticles for the electrocatalytic formate oxidation reaction. *J. Electroanal. Chem.* **2023**, *936*, 117369.
(38) Liao, Y.; Liu, W.; Jia, W.; Wang, B.; Chen, L.; Huang, K.; Montgomery, M. J.; Qian, J.; Lv, S.; Pfefferle, L. D. Bismuth Sulfide Strongly Coupled to Functionalized MWNTs Hybrids with Improved Thermoelectric Properties. *Adv. Energy Mater.* **2021**, *7*, 2100468.
(39) Ni, J.; Zhao, Y.; Liu, T.; Zheng, H.; Gao, L.; Yan, C.; Li, L. Strongly Coupled Bi_2S_3@CNT Hybrids for Robust Lithium Storage. *Adv. Energy Mater.* **2014**, *4*, 1400798.
(40) Berestok, T.; Chacón-Borrero, J.; Li, J.; Guardia, P.; Cabot, A. Crystalline Magnetic Gels and Aerogels Combining Large Surface Areas and Magnetic Moments. *Langmuir* **2023**, *39*, 3692.
(41) Wang, X.; Han, X.; Du, R.; Xing, C.; Qi, X.; Liang, Z.; Guardia, P.; Arbiol, J.; Cabot, A.; Li, J. Cobalt Molybdenum Nitride-Based Nanosheets for Seawater Splitting. *ACS Appl. Mater. Interfaces* **2022**, *14*, 41924−41933.
(42) Li, M.; Yang, D.; Biendicho, J. J.; Han, X.; Zhang, C.; Liu, K.; Diao, J.; Li, J.; Wang, J.; Heggen, M.; Dunin-Borkowski, R. E.; Wang, J.; Henkelman, G.; Morante, J. R.; Arbiol, J.; Chou, S.-L.; Cabot, A. Enhanced Polysulfide Conversion with Highly Conductive and Electrocatalytic Iodine-Doped Bismuth Selenide Nanosheets in Lithium−Sulfur Batteries. *Adv. Funct. Mater.* **2022**, *32*, 2200529.
(43) Yang, D.; Li, M.; Zheng, X.; Han, X.; Zhang, C.; Jacas Biendicho, J.; Llorca, J.; Wang, J.; Hao, H.; Li, J.; Henkelman, G.; Arbiol, J.; Morante, J. R.; Mitlin, D.; Chou, S.; Cabot, A. Phase Engineering of Defective Copper Selenide toward Robust Lithium−Sulfur Batteries. *ACS Nano* **2022**, *16*, 11102−11114.
(44) Wang, X.; Li, J.; Xue, Q.; Han, X.; Xing, C.; Liang, Z.; Guardia, P.; Zuo, Y.; Du, R.; Balcells, L.; Arbiol, J.; Llorca, J.; Qi, X.; Cabot, A. Sulfate-Decorated Amorphous−Crystalline Cobalt-Iron Oxide Nanosheets to Enhance O−O Coupling in the Oxygen Evolution Reaction. *ACS Nano* **2023**, *17*, 825−836.
(45) Du, R.; Xiao, K.; Li, B.; Han, X.; Zhang, C.; Wang, X.; Zuo, Y.; Guardia, P.; Li, J.; Chen, J.; Arbiol, J.; Cabot, A. Controlled oxygen doping in highly dispersed Ni-loaded g-C_3N_4 nanotubes for efficient photocatalytic H_2O_2 production. *Chem. Eng. J.* **2022**, *441*, 135999.
(46) Wang, X.; Han, X.; Du, R.; Liang, Z.; Zuo, Y.; Guardia, P.; Li, J.; Llorca, J.; Arbiol, J.; Zheng, R.; Cabot, A. Unveiling the role of counter-anions in amorphous transition metal-based oxygen evolution electrocatalysts. *AppL. Catal. B* **2023**, *320*, 121988.
(47) Yang, D.; Liang, Z.; Tang, P.; Zhang, C.; Tang, M.; Li, Q.; Biendicho, J. J.; Li, J.; Heggen, M.; Dunin-Borkowski, R. E.; et al. A High Conductivity 1D π−d Conjugated Metal−Organic Framework with Efficient Polysulfide Trapping-Diffusion-Catalysis in Lithium−Sulfur Batteries. *Adv. Mater.* **2022**, *34*, 2108835.
(48) Zhang, C.; Fei, B.; Yang, D.; Zhan, H.; Wang, J.; Diao, J.; Li, J.; Henkelman, G.; Cai, D.; Biendicho, J. J.; Morante, J. R.; Cabot, A. Robust Lithium−Sulfur Batteries Enabled by Highly Conductive WSe_2-Based Superlattices with Tunable Interlayer Space. *Adv. Funct. Mater.* **2022**, *32*, 2201322.
(49) Wu, G.; Yan, Z.; Wang, X.; Tan, X.; Song, K.; Chen, L.; Guo, Z.; Liu, G.-Q.; Zhang, Q.; Hu, H.; Jiang, J. Optimized Thermoelectric Properties of $Bi_{0.48}Sb_{1.52}Te_3$ through AgCuTe Doping for Low-Grade Heat Harvesting. *ACS Appl. Mater. Interfaces* **2021**, *13*, 57514−57520.
(50) Xin, C.; Fang, Z.; Jiang, S.; Hu, Z.; Zhang, D.; Cassagne, F.; Aigouy, L.; Chen, Z. Solution-processed flexible n-type S-doped Ag_2Se thermoelectric generators for near-ambient-temperature energy harvest. *Mater. Today Energy* **2023**, *33*, 101266.
(51) Kihoi, S. K.; Kahiu, J. N.; Kim, H.; Shenoy, U. S.; Bhat, D. K.; Yi, S.; Lee, H. S. Optimized Mn and Bi co-doping in SnTe based thermoelectric material: A case of band engineering and density of states tuning. *J. Mater. Sci. Technol.* **2021**, *85*, 76−86.
(52) Zhou, Z.; Yang, J.; Jiang, Q.; Luo, Y.; Zhang, D.; Ren, Y.; He, X.; Xin, J. Multiple effects of Bi doping in enhancing the thermoelectric properties of SnTe. *J. Mater. Chem. A* **2016**, *4*, 13171−13175.
(53) Shenoy, U. S.; D, G. K.; Bhat, D. K. Probing of Bi doped GeTe thermoelectrics leads to revelation of resonant states. *J. Alloy. Comp.* **2022**, *921*, 165965.
(54) Hu, L.; Meng, F.; Zhou, Y.; Li, J.; Benton, A.; Li, J.; Liu, F.; Zhang, C.; Xie, H.; He, J. Leveraging Deep Levels in Narrow Bandgap

https://doi.org/10.1021/acsaelm.3c00055
ACS Appl. Electron. Mater. XXXX, XXX, XXX−XXX

$Bi_{0.5}Sb_{1.5}Te_3$ for Record-High zTave Near Room Temperature. *Adv. Funct. Mater.* **2020**, *30*, 2005202.
(55) Zheng, W.; Bi, P.; Liu, F.; Liu, Y.; Shi, J.; Xiong, R.; Wang, Z. High Thermoelectric Performance of Au@ Sb_2Te_3 Heterostructure Derived from the Potential Barriers. *arXiv preprint*, 2018, arXiv:1805.08519.
(56) Ma, Z.; Wang, C.; Chen, Y.; Li, L.; Li, S.; Wang, J.; Zhao, H. Ultra-high thermoelectric performance in SnTe by the integration of several optimization strategies. *Mater. Today Phys.* **2021**, *17*, 100350.
(57) Chen, Z.; Wang, R.; Wang, G.; Zhou, X.; Wang, Z.; Yin, C.; Hu, Q.; Zhou, B.; Tang, J.; Ang, R. Band engineering and precipitation enhance thermoelectric performance of SnTe with Zn-doping. *Chin. Phys. B* **2018**, *27*, No. 047202.
(58) Athithya, S.; Jibri, K. P. M.; Harish, S.; Hayakawa, K.; Kubota, Y.; Ikeda, H.; Hayakawa, Y.; Navaneethan, M.; Archana, J. Probing an enhanced anisotropy Seebeck coefficient and low thermal conductivity in polycrystalline Al doped SnSe nanostructure. *AIP Adv.* **2023**, *13*, No. 015311.
(59) Lin, Y.; Wood, M.; Imasato, K.; Kuo, J. J.; Lam, D.; Mortazavi, A. N.; Slade, T. J.; Hodge, S. A.; Xi, K.; Kanatzidis, M. G.; Clarke, D. R.; Hersam, M. C.; Snyder, G. J. Expression of interfacial Seebeck coefficient through grain boundary engineering with multi-layer graphene nanoplatelets. *Energy Environ. Sci.* **2020**, *13*, 4114−4121.
(60) Zhang, X.; Wang, D.; Wu, H.; Yin, M.; Pei, Y.; Gong, S.; Huang, L.; Pennycook, S. J.; He, J.; Zhao, L.-D. Simultaneously enhancing the power factor and reducing the thermal conductivity of SnTe via introducing its analogues. *Energy Environ. Sci.* **2017**, *10*, 2420−2431.
(61) Alleno, E.; Bérardan, D.; Byl, C.; Candolfi, C.; Daou, R.; Decourt, R.; Guilmeau, E.; Hébert, S.; Hejtmanek, J.; Lenoir, B.; Masschelein, P.; Ohorodnichuk, V.; Pollet, M.; Populoh, S.; Ravot, D.; Rouleau, O.; Soulier, M. Invited Article: A round robin test of the uncertainty on the measurement of the thermoelectric dimensionless figure of merit of $Co_{0.97}Ni_{0.03}Sb_3$. *Rev. Sci. Instrum.* **2015**, *86*, No. 011301.
(62) Wang, H.; Bai, S.; Chen, L.; Cuenat, A.; Joshi, G.; Kleinke, H.; König, J.; Lee, H. W.; Martin, J.; Oh, M.-W.; Porter, W. D.; Ren, Z.; Salvador, J.; Sharp, J.; Taylor, P.; Thompson, A. J.; Tseng, Y. C. International Round-Robin Study of the Thermoelectric Transport Properties of an n-Type Half-Heusler Compoundfrom 300 to 773 K. *J. Electron. Mater.* **2015**, *44*, 4482−4491.
(63) Tian, B.-Z.; Jiang, X.-P.; Chen, J.; Gao, H.; Wang, Z.-G.; Tang, J.; Zhou, D.-L.; Yang, L.; Chen, Z.-G. Low lattice thermal conductivity and enhanced thermoelectric performance of SnTe via chemical electroless plating of Ag. *Rare Met.* **2022**, *41*, 86−95.
(64) Chen, T.; Ming, H.; Zhang, B.; Zhu, C.; Zhang, J.; Zhou, Q.; Li, D.; Xin, H.; Qin, X. Ultralow Thermal Conductivity and Enhanced Figure of Merit for $CuSbSe_2$ via Cd-Doping. *ACS Appl. Energy Mater.* **2021**, *4*, 1637−1643.
(65) Cheng, Y.; Yang, J.; Luo, Y.; Li, W.; Vtyurin, A.; Jiang, Q.; Dunn, S.; Yan, H. Enhancement of Thermoelectric Performance in $Bi_{0.5}Sb_{1.5}Te_3$ Particulate Composites Including Ferroelectric $BaTiO_3$ Nanodots. *ACS Appl. Mater. Interfaces* **2022**, *14*, 37204−37212.
(66) Dalmases, M.; Ibáñez, M.; Torruella, P.; Fernàndez-Altable, V.; López-Conesa, L.; Cadavid, D.; Piveteau, L.; Nachtegaal, M.; Llorca, J.; Ruiz-González, M. L.; Estradé, S.; Peiró, F.; Kovalenko, M. V.; Cabot, A.; Figuerola, A. Synthesis and Thermoelectric Properties of Noble Metal Ternary Chalcogenide Systems of Ag−Au−Se in the Forms of Alloyed Nanoparticles and Colloidal Nanoheterostructures. *Chem. Mater.* **2016**, *28*, 7017−7028.
(67) Duan, H. Z.; Li, Y. L.; Zhao, K. P.; Qiu, P. F.; Shi, X.; Chen, L. D. Ultra-Fast Synthesis for Ag_2Se and CuAgSe Thermoelectric Materials. *JOM* **2016**, *68*, 2659−2665.
(68) Chen, J.; Sun, Q.; Bao, D.; Tian, B.-Z.; Wang, Z.; Tang, J.; Zhou, D.; Yang, L.; Chen, Z.-G. Simultaneously enhanced strength and plasticity of Ag_2Se-based thermoelectric materials endowed by nano-twinned CuAgSe secondary phase. *Acta Mater.* **2021**, *220*, 117335.
(69) Lei, Y.; Liu, W.; Zhou, X.; Luo, J.; Zhang, C.; Su, X.; Tan, G.; Yan, Y.; Tang, X. The electronic-thermal transport properties and the exploration of magneto-thermoelectric properties and the Nernst thermopower of $Ag_{2(1+x)}Se$. *J. Solid State Chem.* **2020**, *288*, 121453.
(70) Chen, J.; Yuan, H.; Zhu, Y.-K.; Zheng, K.; Ge, Z.-H.; Tang, J.; Zhou, D.; Yang, L.; Chen, Z.-G. Ternary $Ag_2Se_{1-x}Te_x$: A Near-Room-Temperature Thermoelectric Material with a Potentially High Figure of Merit. *Inorg. Chem.* **2021**, *60*, 14165−14173.

https://doi.org/10.1021/acsaelm.3c00055
ACS Appl. Electron. Mater. XXXX, XXX, XXX−XXX